AAAS
Research
Volume 2020, Article ID 6375171, 8 pages
https://doi.org/10.34133/2020/6375171

Research
A SCIENCE PARTNER JOURNAL

Research Article

Machine Learning Chemical Guidelines for Engineering Electronic Structures in Half-Heusler Thermoelectric Materials

Maxwell T. Dylla,[1] Alexander Dunn,[2,3] Shashwat Anand,[1] Anubhav Jain,[3] and G. Jeffrey Snyder[1]

[1]*Department of Materials Science and Engineering, Northwestern University, IL 60208, USA*
[2]*Department of Materials Science and Engineering, UC Berkeley, CA 94720, USA*
[3]*Lawrence Berkeley National Laboratory, Energy Technologies Area, CA 94720, USA*

Correspondence should be addressed to G. Jeffrey Snyder; jeff.snyder@northwestern.edu

Received 13 January 2020; Accepted 2 March 2020; Published 22 April 2020

Copyright © 2020 Maxwell T. Dylla et al. Exclusive Licensee Science and Technology Review Publishing House. Distributed under a Creative Commons Attribution License (CC BY 4.0).

Half-Heusler materials are strong candidates for thermoelectric applications due to their high weighted mobilities and power factors, which is known to be correlated to valley degeneracy in the electronic band structure. However, there are over 50 known semiconducting half-Heusler phases, and it is not clear how the chemical composition affects the electronic structure. While all the n-type electronic structures have their conduction band minimum at either the Γ- or X-point, there is more diversity in the p-type electronic structures, and the valence band maximum can be at either the Γ-, L-, or W-point. Here, we use high throughput computation and machine learning to compare the valence bands of known half-Heusler compounds and discover new chemical guidelines for promoting the highly degenerate W-point to the valence band maximum. We do this by constructing an "orbital phase diagram" to cluster the variety of electronic structures expressed by these phases into groups, based on the atomic orbitals that contribute most to their valence bands. Then, with the aid of machine learning, we develop new chemical rules that predict the location of the valence band maximum in each of the phases. These rules can be used to engineer band structures with band convergence and high valley degeneracy.

1. Introduction

High thermoelectric performance requires a high thermoelectric quality factor which is proportional to the weighted mobility, μ_W, divided by the lattice thermal conductivity, κ_L [1]. High weighted mobility, which is correlated to high peak power factor, makes p-type half-Heusler materials strong candidates for thermoelectric applications. These materials owe their high weighted mobilities and high power factors to weak electron-phonon coupling and high valley degeneracy imposed by the symmetry of the Brillouin zone [2–6]. However, there are over 50 known semiconducting half-Heusler compounds [7], and it is not clear how the chemical composition affects the electronic structure. In recent work, machine learning has become a powerful tool for engineering complex properties in cases where the known physical trends are exhausted, but there are many features left to understand [8–13]. Simple models, driven by domain knowledge, are especially useful for discovering ways to engineer these properties, even when there are small amounts of available data [14, 15]. In this work, we use machine learning to develop simple models that explain the electronic structures of half-Heusler phases.

To begin to understand electronic structure in the half-Heusler family, we calculated the electronic structures' semiconducting (18 valence electrons) phases using density functional theory (DFT). We chose stable phases reported in the Inorganic Crystal Structure Database (ICSD) alongside 10 phases predicted stable (see Methods) in previous studies from DFT calculations [3, 16, 17]. To quantitatively compare the calculated phases, we decomposed their near band-edge electronic structures into their chemical components—atomic orbitals. For domain experts, atomic orbitals are a powerful basis for interpreting electronic

structure [18–21]. For example, small variations in orbital character (*s*/*p*/*d*) explain whether diamond-like semiconductors have direct or indirect band gaps [22]. Based on a chemical map of each phase's atomic orbitals, we find that there are three distinct classes of electronic structures in the half-Heusler family. While all have conduction band minimum at either the *X*-point or the *Γ*-point—there is more variance in the valence bands—the valence band maximum can be at one of three *k*-points in the Brillouin zone. Phases that are intermediates of the extreme cases even have increased valley degeneracy from the energy convergence of multiple *k*-points at the valence band edge. We use machine learning to elucidate how composition affects the relative energies of these *k*-points, which can direct efforts to engineer band structures with high degeneracy and weighted mobility. Similar to the valence balanced rule that predicts the stability of half-Heusler phases [7], we find that a new valence *difference* rule predicts the relative energies of the *k*-points. Instead of considering the total valence electron count (rule for stability), these rules consider the relative valence electron configurations of the elements on each site of the crystal structure (Figure 1).

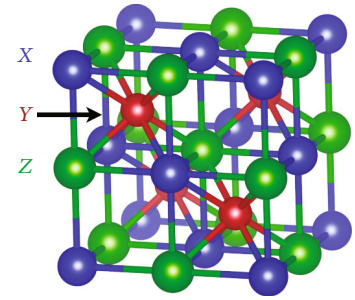


Figure 1: There are three crystallographic sites in the half-Heusler structure: *X* (blue), *Y* (red), and *Z* (green). The *Y*-site is in a body-centered-cubic coordination environment formed by the *X*- and *Z*-sites. The *X*- and *Z*-sites are in tetrahedral coordination environments formed by the *Y*-sites (in the first nearest-neighbor shell) and octahedral coordination environments formed by *X*- and *Z*-sites (in the second nearest-neighbor shell).

2. Classifying Valence-Band-Edge Electronic Structures

When discussing electronic structure in crystalline materials, there are dual aspects to consider. On one hand is the reciprocal space representation—that of electronic band diagrams—where electronic states are indexed by their wave vector, *k*, and band index, *n*. Reciprocal space holds predictive information for many transport properties. For example, materials with low effective mass (m^*) and high valley degeneracy have favorable electronic properties for thermoelectric applications [23]. However, in this four-dimensional space, it is difficult to study systematic changes in electronic structure with varying chemical composition. The complementary perspective of the electronic structure is represented in real space, where the electronic states correspond to combinations of atomic orbitals [19–21]. Atomic orbitals are the components of electronic structures, analogous to how elements are the components of crystal structures. To further the analogy, relevant portions of the electronic structure are described by atomic orbital *compositions*. In this work, we consider the atomic orbital composition of the valence band edge using the projected density of states [24, 25]. The electronic structures are computed using density functional theory with the PBE functional without accounting for spin-orbit coupling effects. We evaluate the fractions of states that would be occupied by holes in the valence bands (see Methods). This composition depends on the electron chemical potential (Fermi level) and temperature, but for consistency across multiple p-type phases, standard conditions were chosen. In this work, the Fermi level is placed at the valence band edge and the temperature is 700 K, which is near the temperature at the experimental peak power factor for half-Heusler materials [3, 4]. Between the three crystallographic sites (*X*/*Y*/*Z*) and three orbital characters (*s*/*p*/*d*), there are nine components to consider. However, only several of the components contribute meaningfully to the valence states, and 97% of the variation in an orbital character is accounted for by the *X*-*d*, *Y*-*d*, and *Z*-*p* components alone (Figure S2 and Table S1). Therefore, the phases can be represented in a Gibbs phase triangle (Figure 2(a)). In contrast to a conventional phase diagram, which represents the stable phases within a composition region, the "orbital phase diagram" represents the diverse electronic structures expressed by phases within a structure family.

There are three emergent classes of valence band electronic structures (indicated by blue, red, and green). The first class of electronic structure (blue) has the valence band maximum at *Γ*, which has a degeneracy of one in the first Brillouin zone (N_{v_k}). To clarify, we are considering the degeneracy imposed by the symmetry of the Brillouin zone, which does not include the number of degenerate bands (N_{v_o}, orbital degeneracy) at that *k*-point ($N_v = N_{v_k} \cdot N_{v_o}$). TiNiSn is an example compound from this class, where the valence band edge is dominated by Ti-*d* states (Figure 2(c)). The second electronic structure class (red) has its valence band maximum at the *L*-point—a degeneracy of four. TaFeSb exemplifies this class, where the band-edge states are dominated by Fe-*d* (Figure 2(d)). In the last class of electronic structure (green), the valence band maximum is at the *W*-point (degeneracy of six). These electronic structures (*e.g.*, NbRhSn in Figure 2(b)) have relatively higher band-edge contributions from *Z*-*p* orbitals, which originates from the states along the *X*-*W* path (green-orange hue). Each of the other electronic structures are hybrids of the three classes. For example, NbCoSn is a hybrid between the *W*-point (green) and *L*-point (red) extremes, with both carrier pockets within 100 meV of the band edge. Irrespective of the electronic structure class, the type of atomic orbitals contributing to each *k*-point (within the first valence band) is similar among all of the half-Heusler materials—the *Γ*-point is dominated by *X*-*d* states, the *L*-point is dominated by *Y*-*d* states, and *Z*-*p* states are mixed into the *X*-*W* path. Therefore, the chemical bonding is similar among all the materials. The primary source of variance among their electronic structures is the relative energies of the *Γ*-, *L*-, and *W*-points, which are linked to the relative energies of their constituent atomic orbitals.

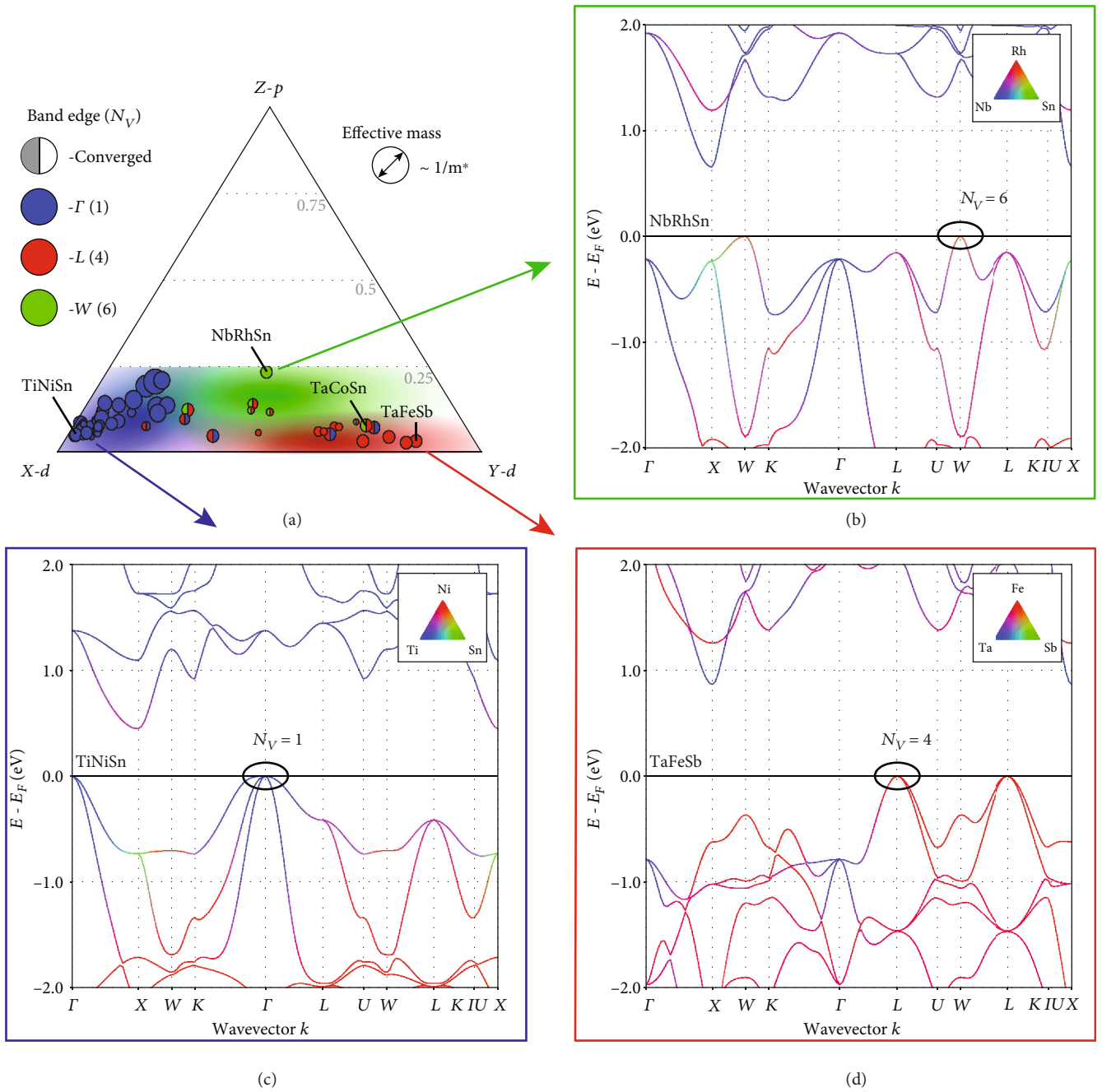


FIGURE 2: (a) The valence band edges of half-Heusler electronic structures are primarily composed of *d* orbitals from the *X*- and *Y*-sites, and secondarily, *p* orbitals from the *Z*-site. The relative contributions of these basis orbitals describe the type of carrier pockets observed in this structure family. (b) Electronic structures with higher concentrations of *Z*-*p* orbitals at the band edge have carrier pockets at the *W*-point with high degeneracy. (c) Phases with valence band edges dominated by *X*-*d* states have carrier pockets at the *Γ*-point, and (d) band edges dominated by *Y*-*d* states have carrier pockets at the *L*-point.

3. Valence Difference Rules for Engineering *Γ*-*L* Carrier Pockets

Engineering the *Γ*-*L* energy offset tunes the valley degeneracy and the thermoelectric performance of half-Heusler materials [4]. The relative energies of the *Γ*- and *L*-points are described by simple, chemical differences between the *X*- and *Y*-species. The dominant, first-order effect is the difference in valence between the *X*- and *Y*-species, which is encoded in their group (column) number on the periodic table. In a linear model, differences in valence account for over 85% of the variation in the *Γ*-*L* energy offset (Figure 3). Compounds with larger differences in valence have valence band maxima at *Γ* (*e.g.*, TiNiSn, where Ni has six more valence electrons than Ti), while compounds with smaller differences in valence have valence band maxima at *L* (*e.g.*, NbFeSb, where Fe has only three more valence electrons than Nb). A second-order descriptor is the difference

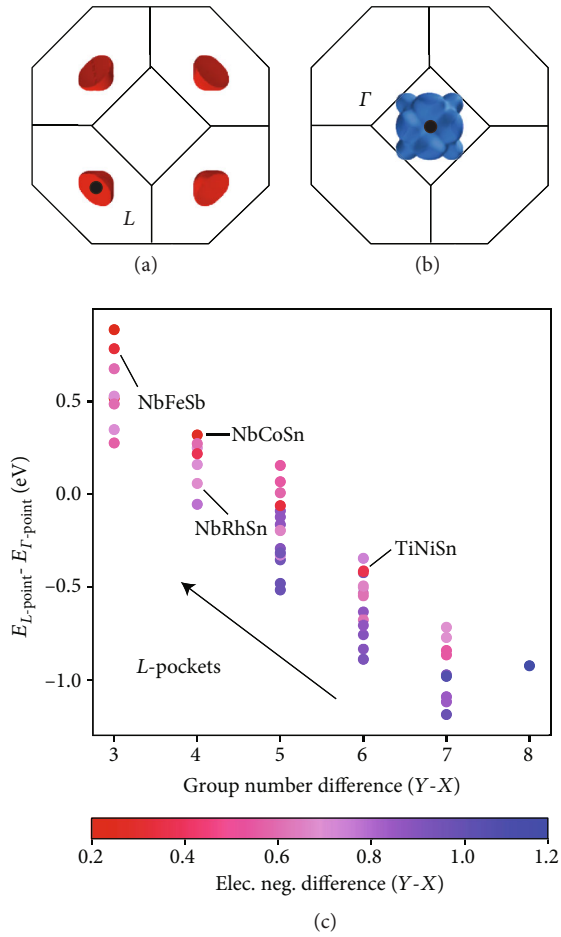


FIGURE 3: (a) Engineering the relative energies of the L-point and (b) the Γ-point controls the degeneracy of half-Heusler materials. (c) The difference in valence electron configuration (encoded in group number) and electronegativity of the X- and Y-species determines the energy offset of these k-points.

in Pauling's electronegativity between the X- and Y-species, which can account for differences in the Γ-L energy offset between compounds with isovalent species (*e.g.*, NbCoSn and NbRhSn). Furthermore, elemental characteristics of the Z-species do not improve the prediction of the Γ-L energy offset, likely because the energies are properties of the X- and Y-species orbitals. Recall that the Γ- and L-point states are formed from the X-d and Y-d orbitals.

The valence difference rule extends beyond the semiconducting phases to metastable phases with 17 and 19 valence electrons [26–28], which are p- and n-type metals (Figure S7). For example, while the energy difference between the Γ- and L-points is nearly zero for TiCoSb, the Γ-pocket dominates the valence band maximum in the Ni-substituted analog; TiNiSb has a larger valence difference and 19 valence electrons. Conversely, in the Fe-substituted analog, the L-pocket dominates; TiFeSb has 17 valence electrons and a smaller difference in valence. While TiNiSb and TiFeSb are not stable themselves, there are implications for forming solid solutions between TiCoSb and either of the metallic end-members (electronic doping) [29]—the relative energies of the Γ- and L-points may change.

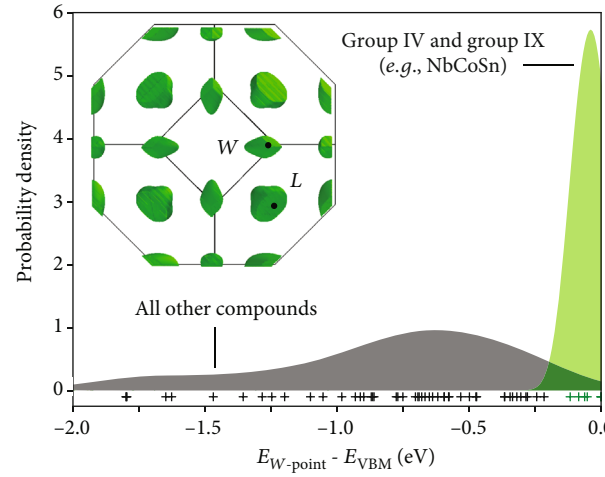


FIGURE 4: The W-point is at or near the valence band maximum for compounds with *both* a group IV element on the Z-site (Sn or Ge) and a group IX on the Y-site (Co, Rh, or Ir). Furthermore, in six of the seven W-pocket materials, the L-point is converged within 100 meV of the band edge (total degeneracy of ten).

4. Engineering Highly Degenerate W-Pocket Materials

Materials that contain *both* group IV (*e.g.*, Sn) and group IX (*e.g.*, Co) elements adopt a distinct class of electronic structure, where the W-point is at or near the valence band edge (Figure 4). In six of these seven phases, the W-point and L-point are both within 100 meV of the valence band edge, effectively converged at 1200 K. The exception to the converged cases is NbRhSn, which is the most extreme example of the W-pocket class. While only Sn- and Ge-containing end-member phases are reported stable in the literature, the calculation of metastable NbCoPb confirms that this valence rule extends beyond Sn- and Ge-containing compounds (Figure S8). Entropy-stabilized solid solutions between NbCoSn and NbCoPb could benefit from reduced lattice thermal conductivity from alloy scattering and retain valley-high degeneracy throughout the solid solution [30–32]. However, the carrier density must be tuned to optimize the thermoelectric transport properties. There are three sites where aliovalent substitution can introduce additional holes in the system and tune the carrier density. We have computed several site-substituted end-members to investigate the potential changes in band structure induced by candidate dopant elements (Figure S8). Substituting on the X- and Y-sites has the expected behavior of tuning the Γ-L energy offset, based on the valence difference rules developed in Section 3.

Substituting Ti on the Nb-site (X-site) raises the relative energy of the Γ point, since the valence difference between Ti and Co is larger than between Nb and Co. Introducing Fe on the Co-site (Y-site) has the opposite effect, and pushes the L-point above the W-point, unconverging the bands. However, substituting In on the Sn-site (Z-site) has an entirely new effect. In NbCoIn, the X-point is at the valence band edge. This compound has an entirely different class of

electronic structure, distinct from the three archetypal band structures identified in Figure 2. The p states from elemental In appear to promote the X-point to the valence band edge. The band structure has a flat and dispersive character between the X- and W-points, which is similar to the band character found in $SrTiO_3$ and some full-Heusler phases [33, 34]. There may be differences in transport properties between materials doped on each of the three sites.

5. Conclusions

We have mapped the electronic structures of semiconducting half-Heusler phases according to the atomic orbital composition of their valence bands. This mapping is termed an orbital phase diagram, and it reveals that there are three well-distinguished classes of electronic structures. The k-points forming the valence band maximum are different for each electronic structure class. The relative energies of these k-points can be controlled using simple rules based on the valence electron configurations of the elemental species. The difference in valence between the X- and Y-species controls the relative energies of the Γ- and L-point energies, while controlling the valence of the Y- and Z-species can lead to the emergence of highly degenerate carrier pockets at the W-point. These rules extend beyond the semiconducting phases, as demonstrated by calculations of metastable 17 and 19 valence electron phases.

These results form a foundation for exploring the space of possible solid solutions in this structure family. Forming solid solutions is incredibly important in the half-Heusler family for suppressing their high lattice thermal conductivities [4, 35–41]. While lattice thermal conductivities in solid solutions are quantitatively described by empirical models [30–32], changes in electronic properties are understood more qualitatively. To the first order, the apparent band structure in a solid solution is a linear interpolation between the end-member electronic structures [42–47]. For example in the Zintl structure family, the band gap and effective mass in n-type $Mg_3Sb_2Mg_3Bi_2$ change linearly with composition between Mg_3Sb_2 and Mg_3Bi_2 [48]. In the III-V semiconductors, the band gap of InAs-GaAs changes linearly as well [49]. In future work on half-Heuslers, the effects of forming solid solutions on the electronic structures could be studied by calculating the backfolded band structures [50, 51] or analyzing their transport properties. Furthermore, the orbital phase diagram technique will be useful for tracking the changes in electronic structure throughout the solid solutions.

6. Methods

6.1. Calculation Details. Electronic structure calculations were carried out using a plane-wave basis (cutoff energy of 520 eV) in the VASP package with PAW pseudopotentials and the PBE functional [25, 52–54]. Spin-orbit coupling corrections were not applied to these calculations. The structural degrees of freedom were relaxed using $12 \times 12 \times 12$ Monkhorst-Pack k-point meshes [55], followed by relaxation of the electronic degrees of freedom using $15 \times 15 \times 15$ meshes. Finally, a non-self-consistent field calculation with $20 \times 20 \times 20$ gamma-centered meshes was used to calculate quantitatively accurate density of states with tetrahedron smearing [56]. In addition, inertial (conductivity) effective masses were calculated using the BoltzTraP package [57]. This set of calculations were performed with the atomate workflow software [58]. The projected density of states and chemical composition were featurized in the matminer package using the SiteDOS and ElementProperty (with pymatgen data) featurizers [59]. The Fermi surfaces of the electronic structures were visualized using the pymatgen package [60]. The most important atomic features for modeling the Γ-L energy offset were determined by ridge regression [61]. The calculations were performed on stable phases reported in the Inorganic Crystal Structure Database (ICSD) alongside 10 phases (HfAsIr, HfBiRh, HfNiPb, HfPdPb, NbSbOs, TaSbOs, TaSnRh, TiAsIr, TiSnPd, and ZrAsIr) predicted stable in previous studies from DFT calculations [3, 16, 17].

6.2. Measuring Electronic Structure Compositions. In p-type semiconductors, charge-transporting holes occupy states in the valence bands according to the distribution function for holes ($h = 1 - f$, where f is the Fermi-Dirac distribution function) [62]. These valence states are ascribed to particular atomic orbitals in the projected density of states (g_i). The number of occupied holes from a particular atomic orbital (p_i) is accumulated from the valence band states (Figure S1).

$$p_i = \int_{\mathrm{VB}} g_i(E) \cdot h(E) \cdot dE. \tag{1}$$

The fractions of atomic-like holes ($x_i = p_i / \Sigma_i p_i$) describe the composition of the system of holes in a particular phase. The composition depends on the Fermi level and the temperature. In this work, the Fermi level is placed at the band edge and the temperature is 700 K. When analyzing conduction bands, the Fermi-Dirac distribution function can replace the hole distribution function.

6.3. Modeling the Γ-L Energy Offset. Regression was used to identify design principles for engineering the Γ-L energy offset. Fivefold crossvalidation was used to score the trained models according to the coefficient of determination (r^2). The model pipeline consisted of standard scaling of the input features (generated from the ElementProperty featurizer with pymatgen data, which was applied to each crystal site) to zero mean and unit variance, followed by ridge regression trained by gradient descent with early stopping. The model scoring was optimized over a grid of tolerance values for early stopping. The optimized model scores and regression weights were collected for a series of regularization strengths (Figure S4/5). As the regularization penalty was decreased, the X- and Y-site group number became the most dominant feature as measured by the regression weights. Ordinary least squares reveals that over 85% of the variation in the energy offset is explained by the difference in group number between the X- and Y-sites alone (Figure S6).

6.4. Modeling the W-Pocket Class. It was observed that compounds with both group IV (*e.g.*, Sn) and group IX (*e.g.*, Co) elements adopt the *W*-pocket type electronic structure. To confirm that this rule describes the distinct class of electronic structure, we compared the distributions of energy offsets between compounds that follow this chemical rule and those that do not (Figure 4). The distributions were estimated using a Gaussian kernel. It can be seen that the two distributions are distinct.

Conflicts of Interest

There are no conflicts of interest to declare.

Acknowledgments

M.T.D. and G.J.S. acknowledge support from the National Science Foundation (DMREF-1333335 and DMREF-1729487). S.A. and G.J.S. acknowledge the U.S. Department of Energy, Office of Energy Efficiency and Renewable Energy (EERE) program "Accelerated Discovery of Compositionally Complex Alloys for Direct Thermal Energy Conversion" (DOE award DE-AC02-76SF00515). A.D and A.J. were supported by the United States Department of Energy, Office of Basic Energy Sciences, Early Career Research Program under award DE-AC02-05CH11231, which funds Lawrence Berkeley National Laboratory. This research used resources of the National Energy Research Scientific Computing Center (NERSC), a U.S. Department of Energy Office of Science User Facility operated under Contract No. DE-AC02-05CH11231.

Supplementary Materials

I. Measuring electronic structure compositions. II. Regression of Γ-L offset. III. Metastable compound calculations. IV. Band structures of the 18 electron half-Heuslers *(Supplementary Materials)*

References

[1] K. Kamoto and T. Mori, Eds., "Thermoelectric Nanomaterials: Materials Design and Applications," in *Springer series in materials science No. Volume 182*, Springer, Heidelberg; New York, 2013, oCLC: ocn857523120.

[2] J. Zhou, H. Zhu, T.-H. Liu et al., "Large thermoelectric power factor from crystal symmetry-protected non- bonding orbital in half-Heuslers," *Nature Communications*, vol. 9, no. 1, pp. 1721–1729, 2018.

[3] H. Zhu, J. Mao, Y. Li et al., "Discovery of TaFeSb-based half-Heuslers with high thermoelectric performance," *Nature Communications*, vol. 10, no. 1, pp. 270–278, 2019.

[4] H. Zhu, R. He, J. Mao et al., "Discovery of ZrCoBi based half Heuslers with high thermoelectric conversion efficiency," *Nature Communications*, vol. 9, no. 1, pp. 2497–2499, 2018.

[5] C. Fu, T. Zhu, Y. Liu, H. Xie, and X. Zhao, "Band engineering of high performance p-type FeNbSb based half-Heusler thermoelectric materials for figure of merit zT > 1," *Energy & Environmental Science*, vol. 8, no. 1, pp. 216–220, 2015.

[6] C. Fu, T. Zhu, Y. Pei et al., "High Band Degeneracy Contributes to High Thermoelectric Performance in p-Type Half-Heusler Compounds," *Advanced Energy Materials*, vol. 4, no. 18, p. 1400600, 2014.

[7] S. Anand, K. Xia, V. I. Hegde et al., "A valence balanced rule for discovery of 18-electron half-Heuslers with defects," *Energy & Environmental Science*, vol. 11, no. 6, pp. 1480–1488, 2018.

[8] L. Ward, A. Agrawal, A. Choudhary, and C. Wolverton, "A general-purpose machine learning framework for predicting properties of inorganic materials," *npj Computational Materials*, vol. 2, no. 1, 2016.

[9] K. T. Butler, D. W. Davies, H. Cartwright, O. Isayev, and A. Walsh, "Machine learning for molecular and materials science," *Nature*, vol. 559, no. 7715, pp. 547–555, 2018.

[10] A. Mansouri Tehrani, A. O. Oliynyk, M. Parry et al., "Machine Learning Directed Search for Ultraincompressible, Superhard Materials," *Journal of the American Chemical Society*, vol. 140, no. 31, pp. 9844–9853, 2018.

[11] J. C. Mauro, "Decoding the glass genome," *Current Opinion in Solid State and Materials Science*, vol. 22, no. 2, pp. 58–64, 2018.

[12] V. Stanev, C. Oses, A. G. Kusne et al., "Machine learning modeling of superconducting critical temperature," *npj Computational Materials*, vol. 4, no. 1, 2018.

[13] P. Avery, X. Wang, C. Oses et al., "Predicting superhard materials via a machine learning informed evolutionary structure search," *npj Computational Materials*, vol. 5, no. 1, 2019.

[14] N. Wagner and J. M. Rondinelli, "Theory-Guided Machine Learning in Materials Science," *Frontiers in Materials*, vol. 3, 2016.

[15] Y. Zhang and C. Ling, "A strategy to apply machine learning to small datasets in materials science," *npj Computational Materials*, vol. 4, no. 1, 2018.

[16] M. Hellenbrandt, "The Inorganic Crystal Structure Database (ICSD)—Present and Future," *Crystallography Reviews*, vol. 10, no. 1, pp. 17–22, 2004.

[17] R. Gautier, X. Zhang, L. Hu et al., "Prediction and accelerated laboratory discovery of previously unknown 18-electron ABX compounds," *Nature Chemistry*, vol. 7, no. 4, pp. 308–316, 2015.

[18] J. K. Burdett, "From bonds to bands and molecules to solids," *Progress in Solid State Chemistry*, vol. 15, no. 3, pp. 173–255, 1984.

[19] R. Hoffmann, "How Chemistry and Physics Meet in the Solid State," *Angewandte Chemie International Edition in English*, vol. 26, no. 9, pp. 846–878, 1987.

[20] W. A. Harrison, *Electronic Structure and the Properties of Solids: The Physics of the Chemical Bond*, Dover Publications, Mineola, NY, USA, 1989.

[21] P. A. Cox, *The Electronic Structure and Chemistry of Solids*, Oxford University Press, Mineola, NY, USA, 2002.

[22] P. Bogusławski and I. Gorczyca, "Influence of Chemistry on the Energy Band Structure: AlAs Versus GaAs," *Acta Physica Polonica A*, vol. 80, no. 3, pp. 433–436, 1991.

[23] Z. M. Gibbs, F. Ricci, G. Li et al., "Effective mass and Fermi surface complexity factor from ab initio band structure calculations," *npj Computational Materials*, vol. 3, no. 1, 2017.

[24] P. E. Blochl, "Projector augmented-wave method," *Physical Review B*, vol. 50, no. 24, pp. 17953–17979, 1994.

[25] G. Kresse and J. Furthmuller, "Efficiency of ab-initio total energy calculations for metals and semiconductors using a plane-wave basis set," *Computational Materials Science*, vol. 6, no. 1, pp. 15–50, 1996.

[26] S. Anand, K. Xia, T. Zhu, C. Wolverton, and G. J. Snyder, "Temperature Dependent n-Type Self Doping in Nominally 19-Electron Half-Heusler Thermoelectric Materials," *Advanced Energy Materials*, vol. 8, no. 30, p. 1801409, 2018.

[27] K. Xia, P. Nan, S. Tan et al., "Short-range order in defective half-Heusler thermoelectric crystals," *Energy & Environmental Science*, vol. 12, no. 5, pp. 1568–1574, 2019.

[28] W. G. Zeier, S. Anand, L. Huang et al., "Using the 18-Electron Rule To Understand the Nominal 19-Electron Half-Heusler NbCoSb with Nb Vacancies," *Chemistry of Materials*, vol. 29, no. 3, pp. 1210–1217, 2017.

[29] S. Anand, M. Wood, Y. Xia, C. Wolverton, and G. J. Snyder, "Double Half-Heuslers," *Joule*, vol. 3, no. 5, pp. 1226–1238, 2019.

[30] P. G. Klemens, "Thermal Resistance due to Point Defects at High Temperatures," *Physical Review*, vol. 119, no. 2, pp. 507–509, 1960.

[31] J. Yang, G. P. Meisner, and L. Chen, "Strain field fluctuation effects on lattice thermal conductivity of ZrNiSn-based thermoelectric compounds," *Applied Physics Letters*, vol. 85, no. 7, pp. 1140–1142, 2004.

[32] H. Wang, A. D. LaLonde, Y. Pei, and G. J. Snyder, "The Criteria for Beneficial Disorder in Thermoelectric Solid Solutions," *Advanced Functional Materials*, vol. 23, no. 12, pp. 1586–1596, 2013.

[33] D. I. Bilc, G. Hautier, D. Waroquiers, G.-M. Rignanese, and P. Ghosez, "Low-Dimensional Transport and Large Thermoelectric Power Factors in Bulk Semiconductors by Band Engineering of Highly Directional Electronic States," *Physical Review Letters*, vol. 114, no. 13, 2015.

[34] M. T. Dylla, S. D. Kang, and G. J. Snyder, "Effect of Two-Dimensional Crystal Orbitals on Fermi Surfaces and Electron Transport in Three-Dimensional Perovskite Oxides," *Angewandte Chemie*, vol. 131, no. 17, pp. 5557–5566, 2019.

[35] A. Tavassoli, F. Failamani, A. Grytsiv et al., "On the Half-Heusler compounds $Nb_{1-x}\{Ti,Zr,Hf\}_xFeSb$: Phase relations, thermoelectric properties at low and high temperature, and mechanical properties," *Acta Materialia*, vol. 135, pp. 263–276, 2017.

[36] C. Fu, S. Bai, Y. Liu et al., "Realizing high figure of merit in heavy-band *p* -type half-Heusler thermoelectric materials," *Nature Communications*, vol. 6, no. 1, 2015.

[37] E. Rausch, B. Balke, S. Ouardi, and C. Felser, "Enhanced thermoelectric performance in the p-type half-Heusler (Ti/Zr/Hf)CoSb0.8Sn0.2system via phase separation," *Physical Chemistry Chemical Physics*, vol. 16, no. 46, pp. 25258–25262, 2014.

[38] R. He, H. S. Kim, Y. Lan, D. Wang, S. Chen, and Z. Ren, "Investigating the thermoelectric properties of p-type half-Heusler Hfx(ZrTi)1−xCoSb0.8Sn0.2by reducing Hf concentration for power generation," *RSC Advances*, vol. 4, no. 110, pp. 64711–64716, 2014.

[39] S. R. Culp, J. W. Simonson, S. J. Poon, V. Ponnambalam, J. Edwards, and T. M. Tritt, "(Zr,Hf)Co(Sb,Sn) half-Heusler phases as high-temperature (>700°C) p-type thermoelectric materials," *Applied Physics Letters*, vol. 93, no. 2, article 022105, 2008.

[40] S. R. Culp, S. J. Poon, N. Hickman, T. M. Tritt, and J. Blumm, "Effect of substitutions on the thermoelectric figure of merit of half-Heusler phases at 800 °C," *Applied Physics Letters*, vol. 88, no. 4, article 042106, 2006.

[41] J. Yu, C. Fu, Y. Liu et al., "Unique Role of Refractory Ta Alloying in Enhancing the Figure of Merit of NbFeSb Thermoelectric Materials," *Advanced Energy Materials*, vol. 8, no. 1, p. 1701313, 2018.

[42] I. T. Witting, T. C. Chasapis, F. Ricci et al., "The Thermoelectric Properties of Bismuth Telluride," *Advanced Electronic Materials*, vol. 5, no. 6, p. 1800904, 2019.

[43] M. Wood, U. Aydemir, S. Ohno, and G. J. Snyder, "Observation of valence band crossing: the thermoelectric properties of CaZn2Sb2–CaMg2Sb2solid solution," *Journal of Materials Chemistry A*, vol. 6, no. 20, pp. 9437–9444, 2018.

[44] W. Li, L. Zheng, B. Ge et al., "Promoting SnTe as an Eco-Friendly Solution for p-PbTe Thermoelectric via Band Convergence and Interstitial Defects," *Advanced Materials*, vol. 29, no. 17, p. 1605887, 2017.

[45] J. Zhang, L. Song, G. K. H. Madsen et al., "Designing high-performance layered thermoelectric materials through orbital engineering," *Nature Communications*, vol. 7, no. 1, 2016.

[46] J. He, X. Tan, J. Xu et al., "Valence band engineering and thermoelectric performance optimization in SnTe by Mn-alloying via a zone-melting method," *Journal of Materials Chemistry A*, vol. 3, no. 39, pp. 19974–19979, 2015.

[47] Y. Pei, H. Wang, and G. J. Snyder, "Band Engineering of Thermoelectric Materials," *Advanced Materials*, vol. 24, no. 46, pp. 6125–6135, 2012.

[48] K. Imasato, S. D. Kang, S. Ohno, and G. J. Snyder, "Band engineering in Mg3Sb2by alloying with Mg3Bi2for enhanced thermoelectric performance," *Materials Horizons*, vol. 5, no. 1, pp. 59–64, 2018.

[49] C. B. Geller, W. Wolf, S. Picozzi et al., "Computational band-structure engineering of III–V semiconductor alloys," *Applied Physics Letters*, vol. 79, no. 3, pp. 368–370, 2001.

[50] P. V. C. Medeiros, S. S. Tsirkin, S. Stafstrom, and J. Bjork, "Unfolding spinor wave functions and expectation values of general operators: Introducing the unfolding-density operator," *Physical Review B*, vol. 91, no. 4, 2015.

[51] P. V. C. Medeiros, S. Stafström, and J. Björk, "Effects of extrinsic and intrinsic perturbations on the electronic structure of graphene: Retaining an effective primitive cell band structure by band unfolding," *Physical Review B*, vol. 89, no. 4, 2014.

[52] G. Kresse and J. Furthmüller, "Efficient iterative schemes forab initiototal-energy calculations using a plane-wave basis set," *Physical Review B*, vol. 54, no. 16, pp. 11169–11186, 1996.

[53] J. P. Perdew, K. Burke, and M. Ernzerhof, "Generalized Gradient Approximation Made Simple," *Physical Review Letters*, vol. 77, no. 18, pp. 3865–3868, 1996.

[54] G. Kresse and D. Joubert, "From ultrasoft pseudopotentials to the projector augmented-wave method," *Physical Review B*, vol. 59, no. 3, pp. 1758–1775, 1999.

[55] H. J. Monkhorst and J. D. Pack, "Special points for Brillouin-zone integrations," *Physical Review B*, vol. 13, no. 12, pp. 5188–5192, 1976.

[56] P. E. Blöchl, O. Jepsen, and O. K. Andersen, "Improved tetrahedron method for Brillouin-zone integrations," *Physical Review B*, vol. 49, no. 23, pp. 16223–16233, 1994.

[57] G. K. Madsen and D. J. Singh, "BoltzTraP. A code for calculating band-structure dependent quantities," *Computer Physics Communications*, vol. 175, no. 1, pp. 67–71, 2006.

[58] K. Mathew, J. H. Montoya, A. Faghaninia et al., "Atomate: A high-level interface to generate, execute, and analyze computational materials science workflows," *Computational Materials Science*, vol. 139, pp. 140–152, 2017.

[59] L. Ward, A. Dunn, A. Faghaninia et al., "Matminer: An open source toolkit for materials data mining," *Computational Materials Science*, vol. 152, pp. 60–69, 2018.

[60] S. P. Ong, W. D. Richards, A. Jain et al., "Python Materials Genomics (pymatgen): A robust, open-source python library for materials analysis," *Computational Materials Science*, vol. 68, pp. 314–319, 2013.

[61] F. Pedregosa, G. Varoquaux, A. Gramfort et al., *Machine learning in Python, 6*.

[62] N. W. Ashcroft and N. D. Mermin, *Solid State Physics*, Holt, Rinehart and Winston, New York, NY, USA, 1976.